AGU PUBLICATIONS

JGR

Journal of Geophysical Research: Space Physics

RESEARCH ARTICLE
10.1002/2017JA025018

Key Points:
- Given a broadband stimulus, it is the natural fast waveguide modes which drive Alfvén resonances
- Resonances of significant amplitude can form at extremely inclined angles (intermediate polarizations)
- Resonance location and structure is fairly insensitive to the form of the driver

Correspondence to:
T. Elsden,
te55@st-andrews.ac.uk

Citation:
Elsden, T., & Wright, A. N. (2018). The broadband excitation of 3-D Alfvén resonances in a MHD waveguide. *Journal of Geophysical Research: Space Physics*, *123*. https://doi.org/10.1002/2017JA025018

Received 17 NOV 2017
Accepted 2 JAN 2018
Accepted article online 16 JAN 2018

The Broadband Excitation of 3-D Alfvén Resonances in a MHD Waveguide

T. Elsden[1] **and A. N. Wright**[1]

[1]Department of Mathematics and Statistics, University of St Andrews, St Andrews, UK

Abstract This paper considers the resonant coupling of fast and Alfvén magnetohydrodynamic (MHD) waves. We perform numerical simulations of the time-dependent excitation of Alfvén resonances in a dipole magnetic field, with nonuniform density providing a 3-D equilibrium. Wright and Elsden (2016) showed that in such a system where the poloidal and toroidal Alfvén eigenfrequencies are different, the resonance can have an intermediate polarization, between poloidal and toroidal. We extend this work by driving the system with a broadband rather than monochromatic source. Further, we investigate the effect of azimuthal inhomogeneity on the resonance path. It is found that when exposed to a broadband driver, the dominant frequencies are the fast waveguide eigenfrequencies, which act as the drivers of Alfvén resonances. We demonstrate how resonances can still form efficiently with significant amplitudes, even when forced by the medium to have a far from toroidal polarization. Indeed, larger-amplitude resonances can be generated with an intermediate polarization, rather than purely toroidal, as a result of larger gradients in the magnetic pressure formed by the azimuthal inhomogeneity. Importantly, the resonance structure is shown to be independent of the different forms of driving, meaning their locations and orientations may be used to infer properties of the equilibrium. However, the amplitude of the FLRs are sensitive to the spatial structure and frequency spectrum of the magnetopause driving. These results have implications for the structure of field line resonances (FLRs) in Earth's magnetosphere, although the focus of this paper is on the underlying physics involved.

1. Introduction

1.1. Historical Context

The resonant coupling between fast and Alfvén magnetohydrodynamic (MHD) waves has received great attention within the space plasma community for many decades. It is a fundamental plasma physics process whereby energy initially resident within the compressional fast mode is transferred at a localized region in space to the incompressible transverse Alfvén mode. In this way, energy which initially propagated across magnetic field lines is converted to energy traveling along field lines. Thus, it is important to understand this process to glean where energy resides in a system at a given time.

Resonances have been shown to play a particularly important role on the Sun and in Earth's magnetosphere (e.g., Ionson, 1978; Southwood, 1974). The theory of resonances has developed somewhat separately in these two areas, (as has MHD wave theory in general) as noted recently by Keiling et al. (2016). This paper pertains to the theory of resonances in Earth's magnetosphere, and hence, we will provide a background into the magnetospheric importance of resonances. However, much of the physics also has relevance in a solar context.

In the magnetosphere, the process of Alfvén resonance excitation is known as field line resonance (FLR). This describes how Alfvén waves, which manifest as standing waves along geomagnetic field lines (Dungey, 1954, 1967), are resonantly driven. The first theoretical models treated this in 1-D, using the ideal, cold (low β) MHD equations, with a radial variation in the Alfvén speed (Chen & Hasegawa, 1974; Southwood, 1974; Tamao, 1965). These authors showed how there exists a unique radial location where the fast mode frequency equals the Alfvén frequency and the modes couple. The development of this theory came about to understand the origin of ultra low frequency (ULF) waves observed by ground magnetometers. Some of these early observations displayed a latitude dependence of ULF waves (e.g., Samson et al., 1971), which the FLR theory could neatly explain.

In the following years, numerical studies greatly advanced our understanding of FLRs in 1-D (Allan et al., 1985; Allan, White, et al., 1986; Allan, Poulter, et al., 1986; Inhester, 1987). These models were extended to 2-D showing how the FLR mechanism was still prevalent (Lee & Lysak, 1989, 1990). The full analytical solution with dependence on two spatial dimensions cemented the mathematics behind FLR excitation in 2-D for the ideal (Wright & Thompson, 1994) and resistive (Tirry & Goossens, 1995) cases.

Resonances in 3-D have received comparatively little attention. This is in part due to the significant difficulty that adding a third spatial dimension creates for the analytical treatment of the problem. Thus, most 3-D studies have considered the numerical solution of the system. Claudepierre et al. (2010) used a global 3-D magnetospheric simulation, driven both monochromatically and with broadband perturbations, to show the existence of FLRs in 3-D in a state-of-the-art simulation. They recently extended this work to consider the inclusion of a plasmasphere in their model, which still resulted in significant, albeit reduced, resonant excitation (Claudepierre et al., 2016). In a similar manner, Ellington et al. (2016) also showed significant resonance excitation within a global simulation. Degeling et al. (2010) considered a compressed dipole model of the magnetosphere again displaying the prevalence of FLR excitation in 3-D. In a solar context, Terradas et al. (2016) have found evidence of 3-D Alfvén resonances in simulations of solar prominences in the process of settling to an equilbrium.

Global models, by their very nature, study numerous aspects of magnetospheric and magnetosheath dynamics and are not optimized specifically for studying FLR formation. For example, such models do not usually use field-aligned coordinates, which in our work allows a much greater resolution of the small scales perpendicular to the background field which develop during FLRs. Further, we have the flexibility to study smaller spatial domains, which provides a far better resolution than current global models. In this regard, Wright and Elsden (2016) and Elsden and Wright (2017) (herein referred to as WE2016 and EW2017) developed a model specifically tailored to the study of resonances in 3-D. They considered a dipole equilibrium in the steady state ($\propto e^{i\omega t}$) (WE2016) and time-dependent (EW2017) regimes. Crucially, in such a curvilinear system, the frequencies of an Alfvén wave with a poloidal polarization (radial field line displacements) and a toroidal polarization (azimuthal field line displacements) are different (Dungey, 1954; Radoski, 1967).

The two key results of WE2016 and EW2017, which are integral to this work, are as follows:

1. Alfvén resonances can form efficiently at some intermediate polarizations (between poloidal and toroidal).
2. The location and structure of such inclined resonances can be predicted by solutions to a modification of the Alfvén wave equation (Singer et al., 1981), to incorporate intermediate polarizations.

1.2. Intentions of This Work

This paper extends the modeling work of WE2016 and EW2017 in two main ways. First, we will consider a broadband rather than monochromatic driver. Many previous works have considered such a driver as a means of modeling the variable solar wind conditions most regularly experienced at Earth (e.g., Claudepierre et al., 2010; Ellington et al., 2016; Wright & Rickard, 1995). Depending on the driver used, this usually leads to the excitation of the global cavity/waveguide modes which then drive FLRs at the corresponding frequencies (Kivelson & Southwood, 1985, 1986; Samson et al., 1992; Wright, 1994).

The second advance is to include a much larger Alfvén frequency gradient in the azimuthal direction than previously. This will force a steeply inclined resonance, that is, an intermediate polarization of the Alfvén wave, which will cross several L shells. The goal is to understand the basic physics of this problem, and if indeed it is possible to sustain such a resonance. This concept is not entirely physically unfounded, given that large dawn-dusk asymmetries in the Alfvén eigenfrequencies were recently found, caused by variations in the radial plasma density profile (Takahashi et al., 2016).

The goal of this work is not to provide another example of resonances within a large-scale global magnetospheric code. Instead, we exaggerate the degree of azimuthal variation in an effort to elucidate the underlying processes as clearly as possible. We provide a well-resolved numerical setup specifically tailored to study resonances, which cleanly resolves the phase mixing length and allows the detailed study of the fine scale structure. The model is introduced in section 2, with the main results presented in section 3 and conclusions given in section 4.

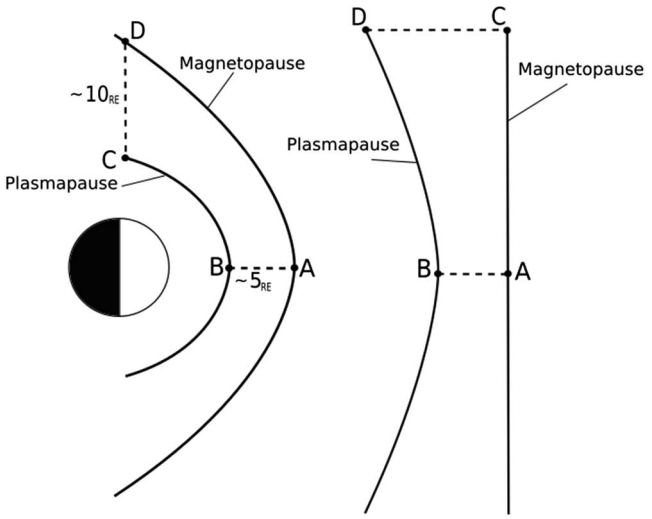

Figure 1. Sketches in the equatorial plane of (left) the real magnetosphere showing key boundaries and distances; (right) our model domain making a comparison to the magnetosphere.

2. Model

2.1. Model—General Details

The model used in this study has been described in depth by WE2016 and EW2017. The first of these works gives a detailed derivation of the coordinate system and resulting equations. The second explains the numerical method and the model domain. To avoid lengthy repetition, all of these details will not be restated, but instead a brief summary with the main details is given in the sections below.

We employ a field-aligned orthogonal coordinate system, which is based on a standard 2-D dipole, chosen specifically to optimize the grid spacing along a field line for numerical efficiency. The coordinates (α, β, γ) represent the radial, azimuthal, and field-aligned directions, respectively. The coordinate system is invariant in the azimuthal (β) direction, and thus, to achieve a 3-D variation in the Alfvén eigenfrequencies which is central to this model, we will vary the Alfvén speed accordingly in this direction.

Figure 1 shows a comparison of the true magnetospheric geometry (left) with our model domain (right) in the equatorial plane. The aim of the model is to capture as much of the basic physics as possible, while retaining simplicity for implementation and numerical efficiency. The principal simplification is to straighten out the azimuthal coordinate and replace it by a Cartesian coordinate β. This is advantageous since the difference in toroidal and poloidal frequencies is increased in the straightened out geometry (WE2016). The locations labeled "A – D" in the left magnetospheric sketch map to their corresponding location in our simulation domain (right-hand sketch). It is important to encapsulate the significant flaring of the true magnetosphere within our simple model. The distance from the plasmapause to magnetopause increases from typically 5_{RE} (noon) to 10_{RE} (dawn/dusk). Since the simulation magnetopause is straight, we achieve the flaring by allowing the plasmapause to move away from the magnetopause by defining a suitable Alfvén speed variation.

We formulate the linearized ideal MHD equations for a cold plasma in the chosen coordinates precisely as listed in EW2017, equations (9) – (13). The resonant singularity is removed from the system by adding a linear drag term to the equation of motion, which limits the smallest-scale size appearing in the domain to maintain appropriate numerical resolution. The system is solved numerically using the second-order leapfrog-trapezoidal finite difference scheme (Rickard & Wright, 1994; Zalesak, 1979). We use a staggered grid to prevent the checkerboard instability and to help with defining derivatives (Trottenberg et al., 2001, p. 314).

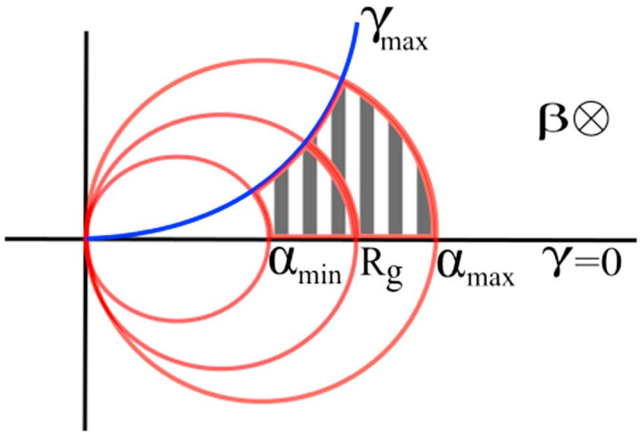

Figure 2. Schematic (not to scale) of the coordinate system and simulation domain (shaded grey region). The red lines represent magnetic field lines (lines of constant α), with the blue line being the upper boundary of the simulation domain (a line of constant γ).

2.2. Model—Specific Details

2.2.1. Boundary Conditions

For clarity, we have reproduced a figure of the simulation domain from EW2017 (their Figure 2) as Figure 2. The boundary conditions are as follows: The radial inner boundary ($\alpha_{\min}$) is taken to be perfectly reflecting, enforced by setting the radial velocity (u_α) to zero there. The outer radial boundary ($\alpha_{\max}$) is driven with a perturbation to the field-aligned magnetic field of the form $b_\gamma \sim \sin^2(\pi t/\tau_d)\cos^2(k_\beta \beta)\cos(k_\gamma \gamma)$, where τ_d is the driving duration and k_β and k_γ are the wave numbers in the β and γ directions, respectively. The driver is turned off after a time of $t = \tau_d = 1.9635$ and is then perfectly reflecting ($b_\gamma = 0$). This "push" to the boundary is designed to model a broadband pulse, in contrast to the monochromatically driven simulations of EW2017. The wavelength and duration of the pulse are important parameters, which will be discussed in detail later. This broadband driving represents the first key change in this work to our previous studies.

A symmetry condition is imposed in the equatorial plane ($\gamma = 0$), such that the complete solution would represent a fundamental mode over the full field line length. To achieve this, the velocity has a node at the ionospheric

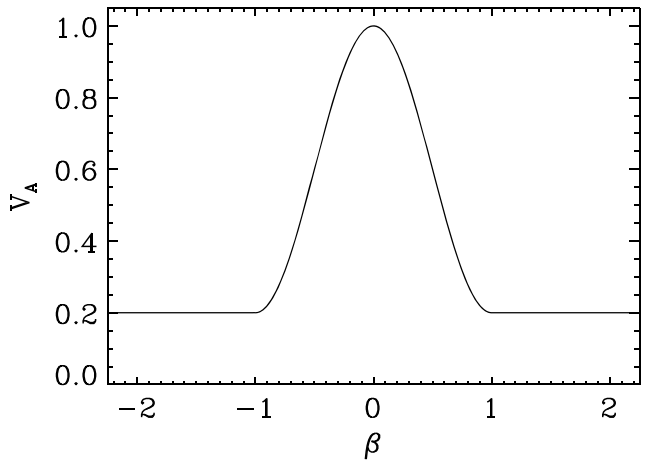

Figure 3. Alfvén speed variation with β.

end of the field line ($\gamma = \gamma_{max}$) and an antinode at the equator ($\gamma = 0$). In azimuth (β), dissipative regions are placed at either end of the waveguide such that perturbations do not significantly reflect and return to the main solution region. This mimics the effect of waves propagating antisunward into the tail.

2.2.2. Varying the Alfvén Speed

The second key new aspect of this work is the variation of the Alfvén speed with azimuth, shown in Figure 3. In the previous works the Alfvén speed also varied with azimuth; however, in this case the gradient of the variation has been significantly increased. This is purely to test the physics of the problem and to answer the question as to whether resonances can be driven in a waveguide with substantial "azimuthal" variation. The Alfvén speed is independent of α (the L shell parameter). However, the natural Alfvén eigenfrequencies vary with α due to the change in magnetic geometry and field line length. This provides the continuum of natural frequencies required for an FLR.

2.2.3. List of Parameter Values

The parameters for the main simulation presented in this paper are set in dimensionless units as follows: The domain extent is $\alpha = 0.3 \rightarrow 1.0$, $\beta = -2.25 \rightarrow 2.25, \gamma = 0.0 \rightarrow 0.455$. In each of the respective directions, 250, 700, and 50 points are taken. The dissipation regions begin at $\beta = \pm 2.0$ and extend to the ends of the domain in β. The dissipation coefficient (ν in equations (9) and (10), EW2017) is 0.1, except in the buffer zones where it increases to 1.0. The duration of the driver is set to $\tau_d = 1.9635$ with a wavelength in β of $\lambda_\beta = 2$. A fundamental mode is taken along the magnetic field with $k_\gamma = 2\pi/\lambda_\gamma = 3.4523$. The total simulation time is $t = 18.51$. The time step is automatically selected for each simulation such that the CFL condition is satisfied throughout the domain (Courant number $C \leq 0.4$). The model as described here typically satisfied total energy continuity to one part in 10^4 at the end of a run. In terms of the resolution relative to the main FLR features, there are at least 20–30 points across a wavelength of say, a component of the velocity, giving 10–15 points across an energy density peak.

3. Simulation Results

3.1. Energy Location and Frequencies

Figure 4 (left) displays the square root of the flux tube energy density (FTED) at time $t = 12.96$ in the simulation. This quantity is formed by integrating the total energy ($\rho u^2/2 + B^2/2\mu_0$) along each field line (i.e., elemental flux tube) in γ and therefore captures all of the energy residing in the Alfvén wave on a given field line at any one time. Figure 4 (middle) shows the square root of the kinetic energy ($\sqrt{\frac{1}{2}\rho u^2}$) in the equatorial plane ($\gamma = 0$) also at time $t = 12.96$. Since we are trying to study inclined resonances, the kinetic energy will display more accurately any energy in the resonances than a single component of the velocity, as is possible with the toroidal component in the 2-D case. The fast mode will make a contribution to the kinetic energy; however, it should be relatively small compared to that of Alfvén waves where FLRs are excited. This is due to the Alfvén wave fields being much larger than the fast wave fields at the resonance location. Hence, we take the localized enhancements in kinetic energy to be indicative of FLRs.

The kinetic energy density and the FTED have different properties. The position of the FTED peak will not change in time because it is based on the total energy. The peaks of the kinetic energy, however, will have a phase motion in time (Wright & Allan, 1996), within the envelope of the FTED maximum. For the particular time chosen, the kinetic energy maximum lies approximately in the center of the FTED envelope. This phase motion will be discussed in section 3.2.

Immediately apparent in Figures 4 (left) and 4 (middle) is the concentration of energy along particular curves, with an overall maximum colored red. The symmetry of the energy distribution is due to the symmetric nature of the driver and domain about $\beta = 0$, while the lack of energy at $\beta = 0$ is caused by the antinode of field-aligned magnetic field (b_γ) there, as also seen in the simulations of Claudepierre et al. (2010) and Ellington et al. (2016). Figures 4 (right) is simply a copy of Figures 4 (middle), but with annotations that will be used in the upcoming analysis. In the following figures, we will present evidence for the displayed energy distribution being caused by the resonant excitation of Alfvén waves. Further, we will explain exactly the path

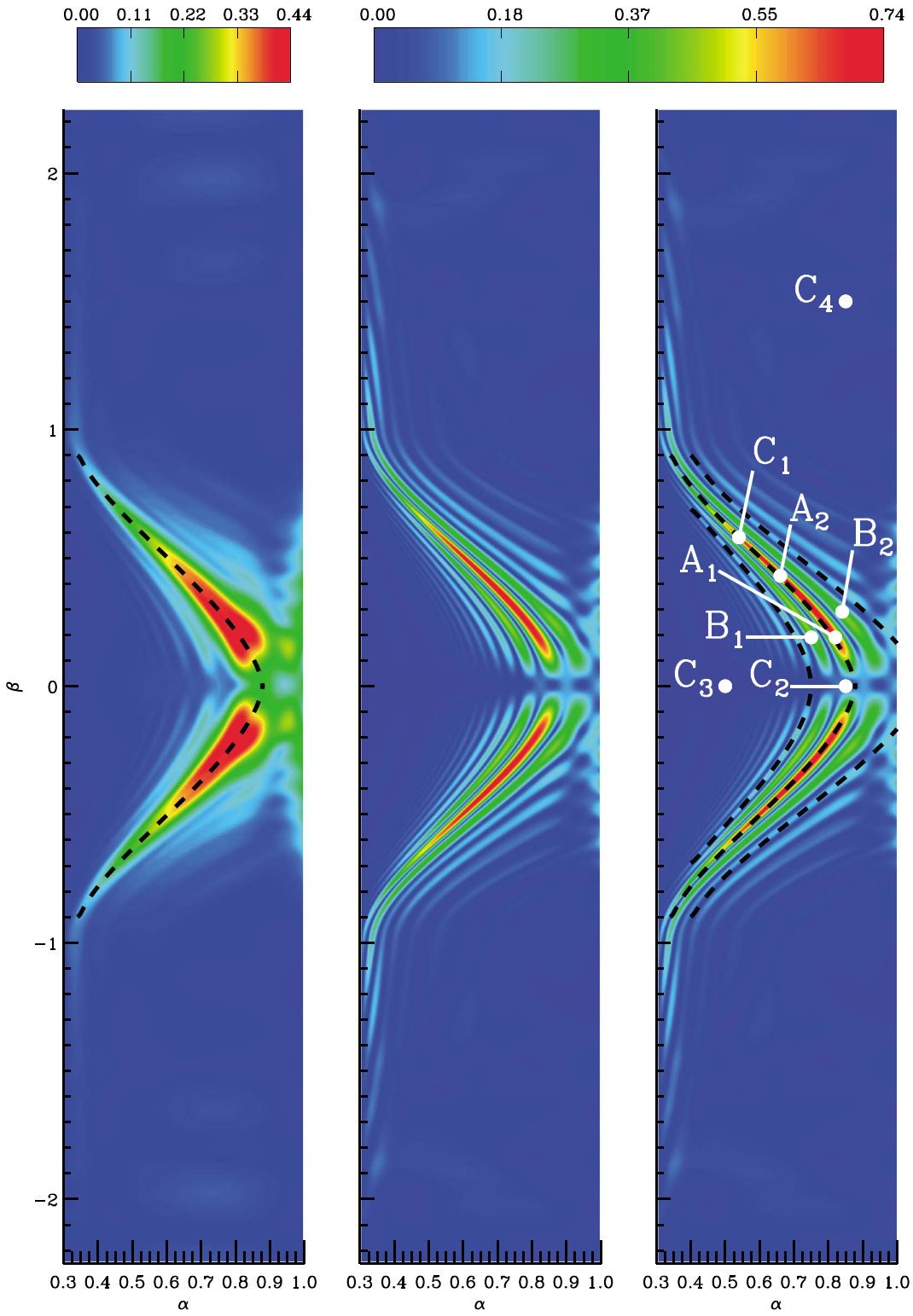

Figure 4. (left) Square root of the flux tube energy density (FTED) at time $t = 12.96$. (middle) Square root of kinetic energy ($\sqrt{\frac{1}{2}\rho u^2}$) in the equatorial plane at time $t = 12.96$. (right) The same as Figure 4 (middle) but with predicted resonant contours for driving frequencies $f = 0.29$ (dashed line in Figure 4, left); $f = 0.39$ (dashed line in Figure 4 (middle); also in Figure 4 (left)) and $f = 0.49$ (dashed line in Figure 4, right) overlaid. Fourier transforms of the wave perturbations at locations $A_1 - C4$ will be later used to interpret the simulation results.

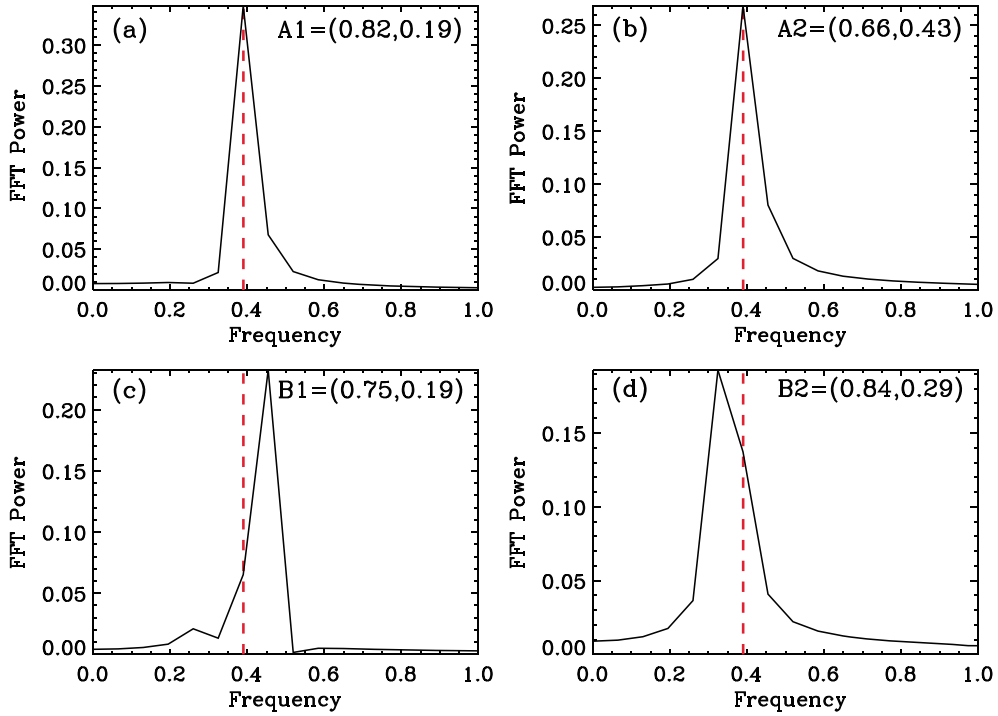

Figure 5. FFTs of u_β at locations corresponding to the annotated Figure 4 (right), as indicated in the top right corner of each figure. The frequency is the cyclic frequency. The red dashed lines are drawn at $f = 0.39$ to aid in the comparison between plots.

that the resonance follows and indeed prove that we have managed to excite resonances where the equilibrium has a steep variation with the azimuthal coordinate.

Figure 5 presents fast Fourier transforms (FFT) of u_β at four locations in the equatorial plane of the simulation domain. These locations are as depicted in Figure 4 (right). The u_β component will be dominated by any resonant response, without containing too much of a contribution from the fast mode. Consider Figures 5a and 5b, comparing points $A_1(0.82, 0.19, 0)$ and $A_2(0.66, 0.43, 0)$. These points were chosen specifically because they appear to lie on the same peak or ridge of the kinetic energy in Figure 4. Indeed, the FFTs reveal that these locations share the same cyclic frequency, $f \sim 0.4$. Thus, the frequency is constant along a ridge in the kinetic energy.

Figures 5c and 5d compare locations $B_1(0.75, 0.19, 0)$ and $B_2(0.84, 0.29, 0)$, chosen as they lie on ridges of the kinetic energy either side of the maximum (again see Figure 4). The dashed red lines on the FFT plots at $f = 0.39$ help to guide the eye and show that the frequencies differ between these locations. At B_1, the frequency is approximately 0.45, while at B_2 it is 0.32. Therefore, the frequency changes between adjacent ridges in the kinetic energy.

Figures 6a and 6b display FFTs of b_γ at locations (a) $C_1(0.85, 0.0, 0.0)$ and (b) $C_2(0.54, 0.58, 0.0)$ as annotated in Figure 4 (right). The b_γ component represents the magnetic pressure and thus is indicative of the fast mode. The two locations are chosen reasonably far apart, but in both the same dominant frequency of $f \sim 0.39$ is apparent. To show that such a frequency is not associated with being on the same ridge of the kinetic energy, panel (d) plots an FFT at point $C_3(0.5, 0.0, 0.0)$ as the dashed line, again showing the same frequency, $f \sim 0.39$. Indeed, an FFT of b_γ anywhere in this central region produces this same frequency and represents the natural waveguide frequency, that is, the natural response of the waveguide to the initial driving.

To understand the effect of dispersion and the spatial coherence of the FFT peak, we consider a point outside of the central region at $C_4(0.85, 1.5, 0.0)$ as annotated in Figure 4. The FFT of b_γ at this point is shown as the solid line in Figure 6d. Surprisingly, the same frequency as the other points is present, albeit with less FFT power. The time series for the points C_3 (dashed) and C_4 (solid) are shown in Figure 6c to help better understand the FFTs. The oscillation at C_3 is of larger amplitude than at C_4 and decays post driving as expected.

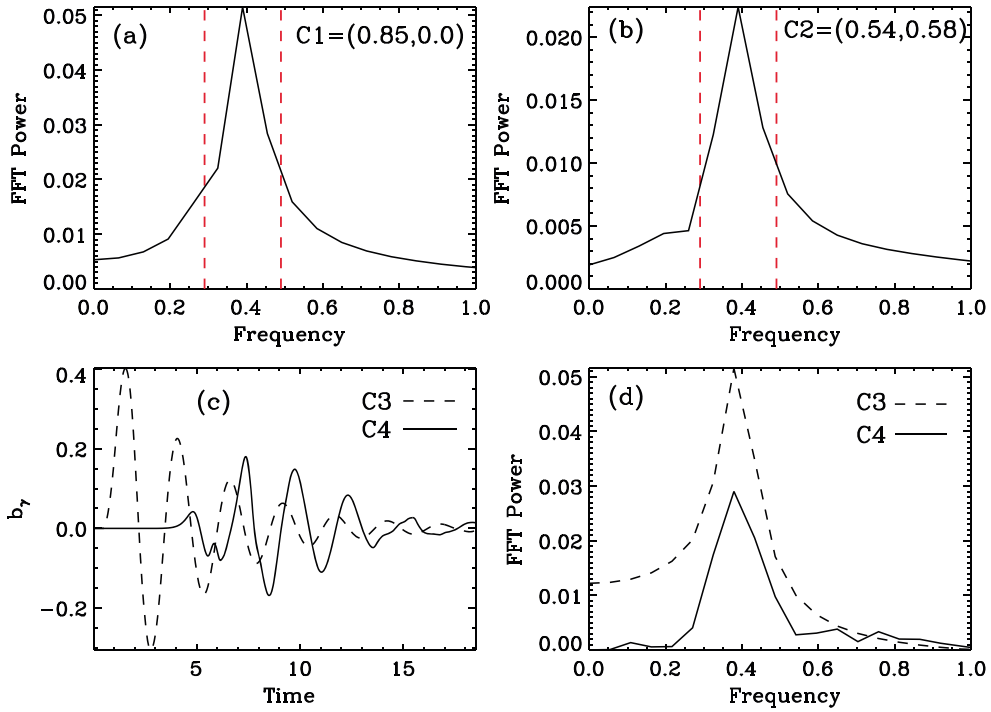

Figure 6. FFTs of b_γ at locations (a) $C_1(0.85, 0.0, 0.0)$ and (b) $C_2(0.54, 0.58, 0.0)$ as annotated in Figure 4. The dashed red lines represent roughly the frequency bandwidth over which there is significant FFT power. (c) Time series of b_γ at $C_3(0.5, 0.0, 0.0)$ (dashed) and $C_4(0.85, 1.5, 0.0)$ (solid), with (d) the corresponding FFTs.

At C_4, the initial perturbation is less coherently established; however, there are three clear periods at the waveguide frequency. We offer an explanation of the uniformity of the b_γ peak in section 3.4.1, after we have studied how the fast mode refracts and establishes the waveguide mode.

The waveguide frequency shown in Figure 6 represents the frequency at which the resonances are being driven. Indeed, comparing Figures 5a and 5b, taken from locations on the line of maximum FTED, with those in Figure 6, they show essentially the same frequency. Therefore, a connection has been made between the global fast mode frequency and the frequency of the dominant "resonant" response.

3.2. Phase Motion of Kinetic Energy Ridges

In this section we consider the phase motion of peaks in the kinetic energy within the resonance envelope, which is identified as the region of enhanced FTED in Figure 4 (left). As briefly mentioned in the previous section, the local maxima of the kinetic energy shown in Figure 4 (middle), will move over the course of one

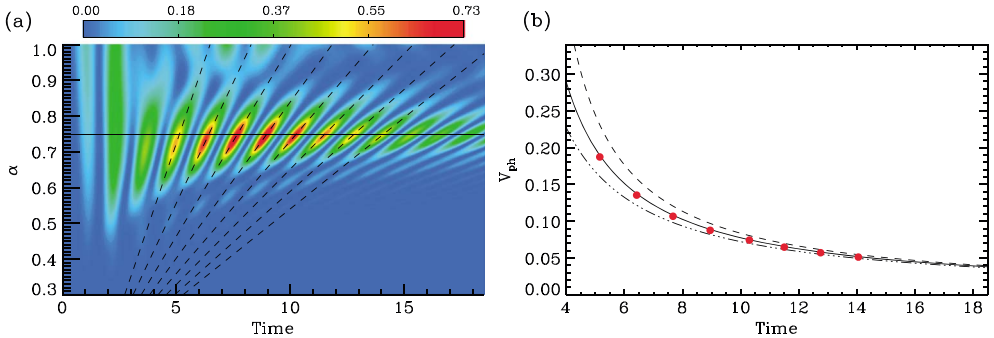

Figure 7. (a) Kinetic energy at $\beta = 0.3$, $\gamma = 0$. The solid line at $\alpha = 0.748$ and the dashed lines are used in the analysis explained in the main text. (b) Phase speed V_{ph} against time at $\alpha = 0.748$, $\beta = 0.3$, $\gamma = 0$. The three lines represent estimates for V_{ph} for different onset times of FLR driving: $t_i = 1.2$, dash-dotted; $t_i = 1.8$, solid; $t_i = 2.4$, dashed. The red dots are phase speed estimates from the data in Figure 7a and were made independently of the inclined dashed lines displayed (which represent a model fit for $t_i = 1.8$, as described in the main text).

period. It is important to study this phase motion to understand how resonances will be observed by a satellite at a point in space (or by ground-based instrumentation) and further, to better interpret the resonance process. In the remainder of this subsection, we analyze the data in Figure 7 as an observer might study real observations and show how details such as the Alfvén frequency gradient and the onset time of driving can be determined.

It is well established that in a system with a gradient in the Alfvén frequency, phase mixing will generate smaller scales over time (Heyvaerts & Priest, 1983), as neighboring field lines with different natural frequencies drift out of phase. A metric for the minimum spatial-scale size is the phase mixing length L_{ph}, which for the $\mathbf{e}_\alpha$ direction can be written as

$$L_{\mathrm{ph}} = \frac{2\pi}{\left(\mathrm{d}\omega_A/\mathrm{d}\alpha\right)(t - t_i)}, \tag{1}$$

(e.g., Mann et al., 1995) where ω_A is the Alfvén frequency and t_i is the time at which the system was set oscillating, that is, the beginning of the phase mixing process. This spatial scale represents the wavelength in the $\mathbf{e}_\alpha$ direction, and thus from this the phase speed is given by

$$V_{\mathrm{ph}} = -\frac{L_{\mathrm{ph}}\omega_A}{2\pi} = -\frac{\omega_A}{\left(\mathrm{d}\omega_A/\mathrm{d}\alpha\right)(t - t_i)}, \tag{2}$$

as shown by Wright et al. (1999) (their equation (4)), Kaneko et al. (2015) (their equation (80)), and Raes et al. (2017) (their equation (10)). We can test the validity of this expression in our simulations by considering the phase motion in time at a constant position in β. Figure 7a displays a color plot of the kinetic energy variation with α and time in the equatorial plane ($\gamma = 0$) at $\beta = 0.3$. This point was chosen only because the kinetic energy peak from Figure 4 (middle) clearly traverses it. Equally, any other such value of β could be chosen for the following analysis. Evident from the plot is the phase motion of the ridges in time; that is, the green/red ridges are inclined to the right indicating that at some later time, the maximum has moved to a different α. This phase motion is to larger α from higher to lower frequencies, in agreement with Wright and Allan (1996) (see their Figure 5). Further evident is the narrowing of the resonance width in α over time, indicated by the convergence of the green ridges around $\alpha \sim 0.75$. The solid line in Figure 7a at $\alpha = 0.748$ will be used to analyze the evolution of V_{ph} in more detail, since all of the maxima (colored red) intersect this line.

We can treat this simulation data as observers and simply measure the gradient of the ridges at the time where they intersect the solid line. This gradient will represent the phase speed and is calculated for eight ridges at the appropriate times. This was done by individually drawing a line through each ridge and measuring its slope. These lines are not shown in Figure 7a, but the value of their gradient is plotted as the red circles in Figure 7b. We describe in the following paragraph how the lines shown in Figure 7a were produced. Further displayed in Figure 7b are estimates of the evolution of the phase speed based upon equation (2) for three different oscillation start times: $t_i = 1.2$, dash-dotted line; $t_i = 1.8$, solid line; $t_i = 2.4$, dashed line. The Alfvén frequency ω_A and its gradient at $\alpha = 0.748$ required for evaluating equation (2) were estimated using time series from the simulation data. (The values of the Alfvén period at $\alpha = 0.7312$, $\alpha = 0.748$, and $\alpha = 0.7704$ were estimated to be 2.51, 2.58, and 2.67, respectively, giving $\omega_A = 2.435$ and $\mathrm{d}\omega_A/\mathrm{d}\alpha = -3.827$ at $\alpha = 0.748$). It is clear that the 'observed' phase speeds can be well accounted for by equation (2), with the initiation time of $t_i = 1.8$ providing the best match.

Given this information, we can return to Figure 7a and draw straight lines emanating from this global start time and attempt to match the gradients of the ridges at $\alpha = 0.748$. As evident from the figure, such lines can be drawn which validates the calculation of t_i using Figure 7b. Indeed, such lines cannot be drawn from any other value of t_i other than 1.8. These lines converge and all intersect at the time $t = 1.8$ (not shown in the figure).

An important question from this analysis is what defines the initiation time t_i? This time represents when phase mixing is initiated, as evident from equations (1) and (2). It can further be thought of as the time at which a coherent fast mode has been established to drive the resonances. This time is likely to depend upon various travel times within the system, some of which may depend upon the location of the resonance. In the case presented, the duration of driving is given by $\tau_d = 1.9635$, as the driver has the dependence $\sin^2(\pi t/\tau_d)$ and so may have a relation to the calculated t_i of 1.8. Further, the natural waveguide frequency of $\omega = 2\pi(0.39) = 2.45$ may also play a role. However, further investigation into this matter is beyond the scope of the present study.

3.3. Resonance Maps

To understand the particular paths that the ridges in kinetic energy trace out in Figure 4, we can construct Resonance Maps. This terminology was introduced by WE2016, to describe the family of solutions to the Alfvén wave equation when traced out in the equatorial plane. The method is discussed by WE2016 and EW2017 but is briefly summarized here.

Equation (23) from WE2016 describes the Alfvén wave equation for an Alfvén wave of arbitrary polarization, and is reproduced below

$$\frac{\partial}{\partial\gamma}\left(\frac{1}{h_\gamma}\frac{\partial U_{\beta'}}{\partial\gamma}\right)+\frac{1}{h_\gamma}\frac{\partial}{\partial\gamma}\left(\ln\left(\frac{h_{\beta'}}{h_{\alpha'}}\right)\right)\frac{\partial U_{\beta'}}{\partial\gamma}+\frac{\omega_A^2}{V_A^2}h_\gamma U_{\beta'}=0, \tag{3}$$

where the dash superscript represents a rotation of the coordinates through an angle θ, such that $\mathbf{e}_{\beta'}$ is the direction aligned with the resonance, ω_A is the Alfvén frequency, V_A is the Alfvén speed, $U_{\beta'}$ is a scaled version of the velocity along the resonance and $h_{\alpha'}$ and $h_{\beta'}$ are the scale factors in the rotated coordinate system. This equation is a generalization of the more familiar equations for the toroidal and poloidal Alfvén waves. The scale factors depend upon the amount of rotation (θ) which coincides with the Alfvén wave velocity perturbation, and hence is the waves polarization. (The toroidal and poloidal Alfvén waves correspond to $\theta = 0$ and $\pi/2$, respectively.) On a given field line, and for a given polarization, the equation may be solved numerically to yield the Alfvén frequency $\omega_A(\alpha,\beta,\theta)$. This relationship can be used to identify the polarization of Alfvén waves that will resonate with a driving frequency ω_d by finding the value of θ for which $\omega_A(\alpha,\beta,\theta)=\omega_d$. Of course, there are locations in the domain where such solutions do not exist, which separates the domain into zones where resonances can or cannot form.

In Figure 8 we have constructed the Resonance Maps for three different driving frequencies; $f = 0.29$, $f = 0.39$, and $f = 0.49$. These frequencies are derived from the FFT of b_γ in Figure 6a. The lower and upper frequencies represent the range of frequencies over which significant power resides in the fast mode, while the middle is the waveguide frequency which drives the dominant resonant response. In each panel we have plotted the Resonant Zone boundaries (red) and representative lines for which any point on a line has a natural Alfvén frequency (given the slope of the line, that is, polarization) matching the particular driving frequency (black).

The Resonant Zone boundaries are constructed as follows: Choose a field line and determine $\omega_A(\alpha,\beta,\theta)$—the Alfvén frequency for different polarizations. Find the maximum value of the Alfvén frequency ($\omega_{\mathrm{Amax}}(\alpha,\beta)$) for this field line. Now find all the field lines for which $\omega_{\mathrm{Amax}}(\alpha,\beta)-\omega_d=0$. This is an equation for a line $\beta(\alpha)$ and corresponds to one of the Resonant Zone boundaries. The other boundary is found in a similar fashion by considering the minimum Alfvén frequency.

For the simple equilibrium magnetic field we consider that the maximum and minimum Alfvén frequencies correspond to the toroidal and poloidal frequencies, respectively. Thus, the Resonant Zone boundaries are constructed by considering the location where, for $\theta = 0$ (toroidal) and $\theta = \pi/2$ (poloidal), the Alfvén frequency matches the driving frequency. Outside of this region, no solutions to the resonant condition exist. This boundary distinction can be understood by observing that black contours enter the toroidal boundary aligned with the β axis and enter the poloidal boundary aligned with the α axis (see also Figure 2 of Klimushkin et al. (1995), where curves with the same properties are considered for a different wave process). It is important to understand that along each black contour, the Alfvén frequency matches the driving frequency if the polarization of the Alfvén wave magnetic or velocity field is oriented tangential to the curve. For our simple choice of background magnetic field, the Alfvén frequency on a given field line is an even function of θ (WE2016), so any point in the Resonant Zone will always have two lines through it, one inclined at $+\theta$ and the other at $-\theta$.

The blue lines in Figure 8 are special members from the family of black lines. They have been emphasized as they correspond to the lines where the simulation should show the most significant energy accumulation and can be identified using the criteria given in WE2016 and EW2017 as follows. In Figure 8 (left) and 8 (middle), the domain contains the extended "2-D" regions for $|\beta|>1$. In these regions the resonance will have a toroidal polarization; hence, the dominant resonance will have to connect to the toroidal boundary for $|\beta|>1$. The blue lines in these panels are exactly such lines. In Figure 8 (righ), the inner simulation boundary intersects the Resonant Zone. Since this boundary is perfectly reflecting ($u_\alpha = 0$), it enforces a toroidal polarization there. This implies that the required contour originates from this intersection with such a polarization.

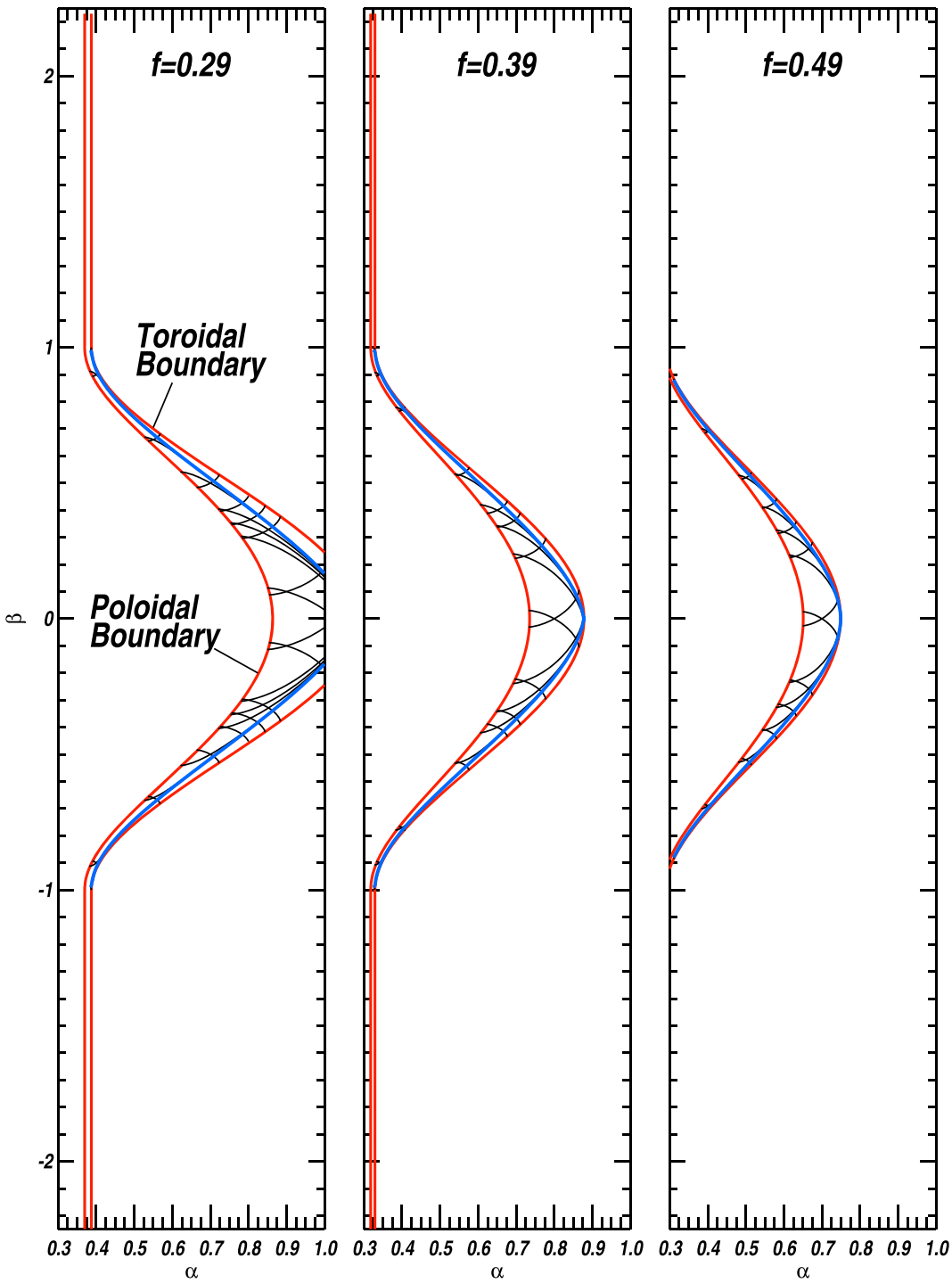

Figure 8. Resonance maps for the driving frequency spectrum: (left) $f = 0.29$; (middle) $f = 0.39$; (right) $f = 0.49$. The red lines are the Resonant Zone bounds as labeled in Figure 8 (left). The black and blue lines are representative solutions to the Alfvén wave equation matching the given driving frequencies, with the blue corresponding to the dominant resonant locations.

The blue line from Figure 8 (middle) (corresponding to the peak of the magnetic pressure FFT) is reproduced as the black dashed line in Figures 4 (left) and 4 (right) (middle line). This line overlies exactly the FTED maximum, showing that the resonance map does accurately predict where resonances will form. The blue lines from Figures 8 (left) and 8 (right) are depicted as the black inner and outer dashed lines in Figure 4 (right). It is of interest how these lines neatly bound the region of enhanced kinetic energy. This confirms that it is the frequency bandwidth of the fast mode (which is driving the resonance) which determines the spatial extent of the resonant response. This further depends upon the variation in the natural Alfvén frequency with α, which explains the narrowing of the Resonant Zones toward smaller α, as the Alfvén frequency varies more rapidly with α there. Indeed, the real magnetosphere would have a similar structure, with larger Resonant Zones at larger L shell. The overall resonance structure is controlled in the simulation by the Alfvén speed profile. The Alfvén speed drops dramatically away from $\beta = 0$, and hence, the resonance is forced to move radially inward to match the driving frequency.

Some of the mathematics and properties of the Resonance Maps we describe here have arisen in a different context in the work of Leonovich and Mazur (1993). They did not consider the resonant coupling of fast and Alfvén waves, but rather the large azimuthal wave number (m) normal mode solutions in an axisymmetric equilibrium. Their model envisaged a pulsating current source in the ionosphere which could resonantly excite a large m poloidal Alfvén wave in the magnetosphere. They go on to suggest that "This [poloidal Alfvén] wave, while traveling across magnetic shells, changes from the poloidal to the toroidal wave. On the magnetic shell, whose frequency of toroidal eigenoscillations coincides with the frequency of the wave concerned, it is totally absorbed due to dissipation in the ionosphere."

These ideas were extended by Klimushkin et al. (1995) to nonaxisymmetric equilibria. What these studies have in common with our work is that they all consider standing Alfvén waves with a given frequency that have small scales perpendicular to the background magnetic field, and these waves can have a polarization anywhere between toroidal and poloidal. These are exactly the properties of resonant Alfvén waves that will result from fast mode driving. Hence, some of the wave operators developed by Leonovich and Mazur (1993) and Klimushkin et al. (1995) could be exploited in future studies of resonant fast-Alfvén wave coupling.

3.4. Gradients in Magnetic Pressure

Resonance Maps are a key tool in explaining where the resonances will form, but they provide no information as to the efficiency of the fast-Alfvén wave coupling. In this regard, we consider how gradients of the magnetic pressure change throughout the domain, given that it is precisely these gradients which drive resonances (e.g., Wright, 1994).

Figure 9a displays a contour plot of b_γ in the equatorial plane at time $t = 2.47$. The red lines overlaid are the same as the blue lines from Figure 8 (middle), representing the location of the dominant resonant response. To consider the importance of the gradient of b_γ, we can introduce a coordinate along the resonance, β', as mentioned in the previous section when discussing equation (3). EW2017 derived expressions for the resonance amplitude for a normal mode in time (their equations (23)–(25)) which are not restated here for brevity. They identified a key component of the resonance amplitude as the directional derivative of b_γ along the resonance, $(1/h_{\beta'})(\partial b_\gamma/\partial\beta')$.

Considering the contour plot in Figure 9a, we first note that the symmetry of the driver and the equilbrium about $\beta = 0$ imply that the directional derivative as given above is zero there. This explains the lack of resonant excitation at $\beta = 0$ in Figure 4. Moving away from this location along the resonance, the directional derivative of b_γ begins to increase. This is evident as the red lines start to rapidly cross contours of b_γ. Referring back to Figure 4, the amplitude is almost constant for a large portion of the peak (extended red maximum). We surmise that the increase of the directional derivative of b_γ along the resonance away from $\beta = 0$ is largely responsible for this spatially extended maximum. There are of course many competing factors involved in the resonance amplitude as highlighted by the formula of EW2017; however, such gradients are clearly important.

It is further worth noting that strong gradients are present elsewhere in the domain. However, only within the Resonant Zone can resonances exist, and hence, these gradients do not drive resonances outside the Resonant Zone. Figures 9b and 9c provide a context to the contour plot, showing the global peaks and troughs of b_γ. Figure 9c (time $t = 5.55$) is approximately one period later than (Figure 9b) ($t = 2.47$). The red regions represent the refraction of perturbations of b_γ due to the inhomogeneity of the medium, and it is precisely this which creates the required gradients to more efficiently drive resonances. These plots emphasize how one

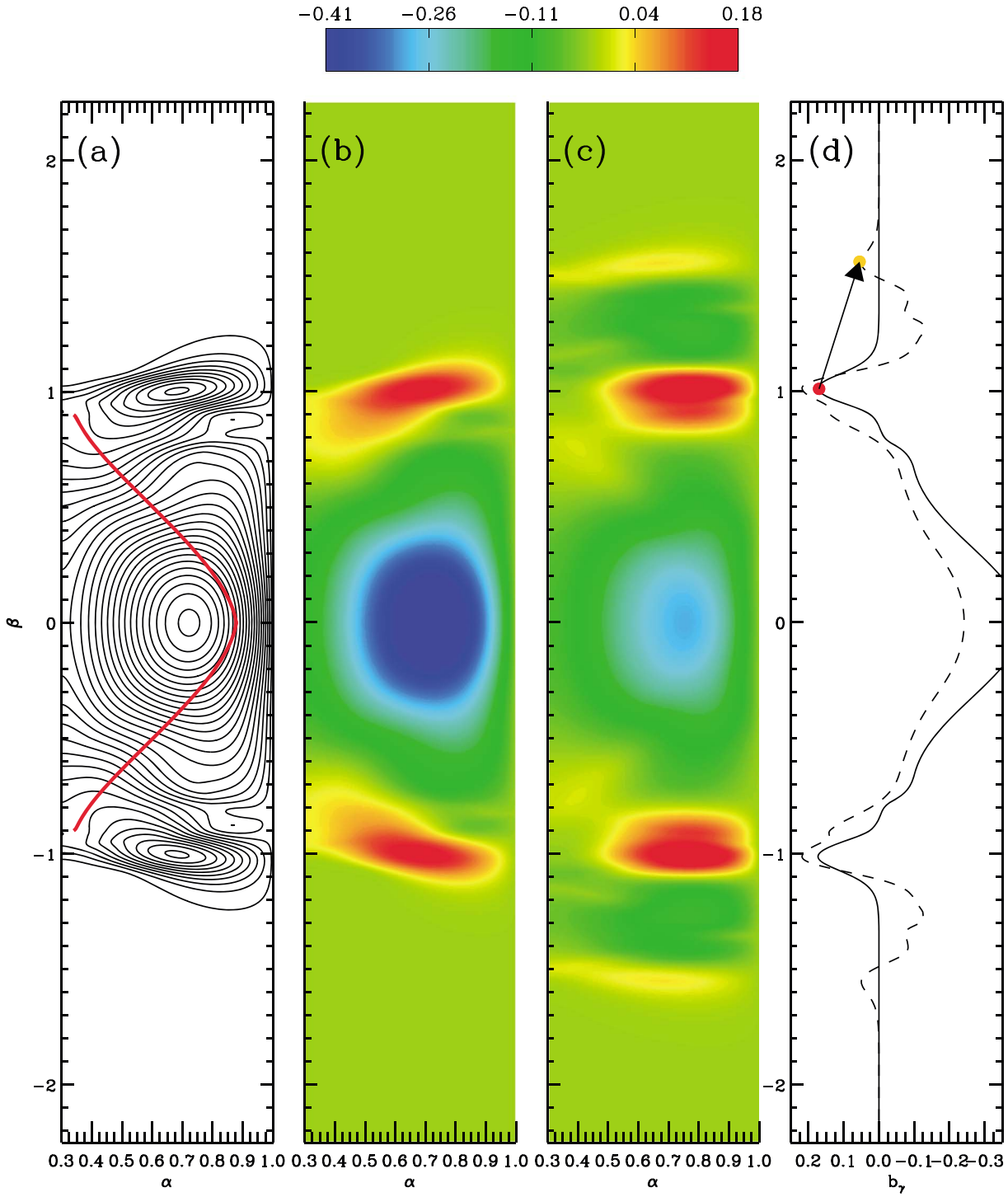

Figure 9. (a) Contour plot of b_γ at time $t = 2.47$ with the main resonant contour from Figure 8 (middle) overplotted in red; (b) color-shaded image of b_γ at $t = 2.47$; (c) color-shaded image of b_γ at $t = 5.55$; (d) plot of b_γ against β at $\alpha = 0.748$. Solid line at $t = 2.47$ (same as Figure 9, middle), dashed line at $t = 5.55$ (same as Figure 9, right). Arrow from red to yellow dot highlights the motion of the peak over one period. Note that all plots are in the equatorial plane.

cycle later the red regions (in Figure 9b) have propagated down the waveguide (to become the yellow regions in Figure 9c, while the central blue region is essentially unchanged, showing the coherency of the driver there. Figure 9d plots $b_\gamma(\beta)$ at $\alpha = 0.748$ with the solid line corresponding to the same time in Figures 9a and 9b), and the dashed to the same time as Figure 9c, which highlights the peaks and troughs present in Figures 9b and 9c. The colored dots together with the arrow added to the peaks on the solid and dashed lines, highlight how the peak has moved down the waveguide (from red dot to yellow) over one period.

3.4.1. Fast Mode Ray Tracing

Figure 9 shows how an enhancement of fast mode energy is trapped in the region $-0.5 < \beta < 0.5$ and pulsates with a period corresponding to the peak FFT power seen at the points C_1, C_2, and C_3 in Figure 4. Hence, the fast mode in this region is essentially a normal mode with a coherent frequency. A complimentary description of waves can also be given in terms of ray tracing, In this formulation, the period of the normal mode corresponds to the bounce time of a wave packet.

We can use the ray tracing perspective to gain some insight into the formulation of the normal mode by simply driving the boundary over a short time such that a localized wave packet is launched from the boundary. This was accomplished by driving the boundary with b_γ as before but with a variation of $\cos^2(k_\beta \beta)$ over $-2 < \beta < 2$, and $\sin^2(\pi t/\tau_d)$ in time with $\tau_d = 0.10472$ for $0 < t < \tau_d$.

Figure 10 displays color-shaded plots of $|b_\gamma|$ in the equatorial plane for three different snapshots in time. Figure 10 (left), at time $t = 0.338$, shows the radially inward propagation of the wavefront. The inhomogeneity of the medium is immediately apparent, as the perturbation in the low Alfvén speed regions ($|\beta| > 1$) has barely moved while the center of the perturbation has propagated to $\alpha \sim 0.7$. Clearly, there has been significant refraction of the wave associated with the nonuniform Alfvén speed.

Figure 10 (middle) at time $t = 0.677$ further emphasizes this refraction, while Figure 10 (right) at time $t = 1.015$ shows how the wave has reflected off the inner boundary and is propagating back to larger α. There are two key points to be made here. First, the refraction demonstrated here is precisely what is required to generate the gradients in b_γ parallel to resonant solution paths. These gradients, as previously mentioned, help to more efficiently drive the resonant coupling. Indeed, even if the driver is completely uniform in beta (i.e., had no inherent gradients) refraction would cause the wave to propagate in a fashion that gradients would develop, and thus facilitate coupling to FLRs. This is very different to 2-D models where the gradients are present in the driver, but not in the equilibrium. In 3-D the equilibrium itself can dictate the scales that gradients occur over. Moreover, these scales can be significantly smaller than any scales present in the driver.

The second key point concerns the reflection of the wave around $\beta = 0$ as can be seen in Figure 10 (right). Wright (1994) discusses the importance of having a coherent driver over many wave cycles to excite large amplitude resonances and surmises that it is the small k_y (small k_β in our model) modes which will achieve this. The structure of the Alfvén speed inhomogeneity in β (Figure 3) provides the scale width over which reflection can occur coherently over several periods to drive the resonances. This width is apparent in Figure 10 (right) after one reflection and gives some insight into the coherence of the magnetic pressure seen throughout the entire simulation domain. A region of trapping occurs around $\beta = 0$ where fast modes waves can bounce in essentially a radial direction, permitting the trapping of the fast mode there. For $|\beta| \sim 0.5$ the wave refracts and forces the wave to propagate down the waveguide. This behavior is dictated by the equilibrium Alfvén speed profile. For $|\beta| < 0.5$ fast energy may be partially trapped, as seen in Figures 9b and 9c providing a coherent pulsing fast mode that gradually decays as energy leaks downtail. This explains why the point C4 in Figure 4 sees the same dominant frequency as C1 – C3.

The competing criteria for the efficiency of the coupling can be listed as follows:

1. How much fast mode energy reaches the resonance? The resonance exists in the evanescent tail of the fast mode, and hence, resonances farther radially inward will be driven by smaller amplitude fast modes.
2. Gradients in magnetic pressure: larger gradients drive larger-amplitude resonances.
3. Coherent driver: fast modes which are persistent in a region where resonances can form are required to efficiently drive resonances.
4. Wave refraction can produce magnetic pressure variations on the scale of the equilibrium inhomogeneity.

We have demonstrated how these four factors all play a competing role in determining how resonances form.

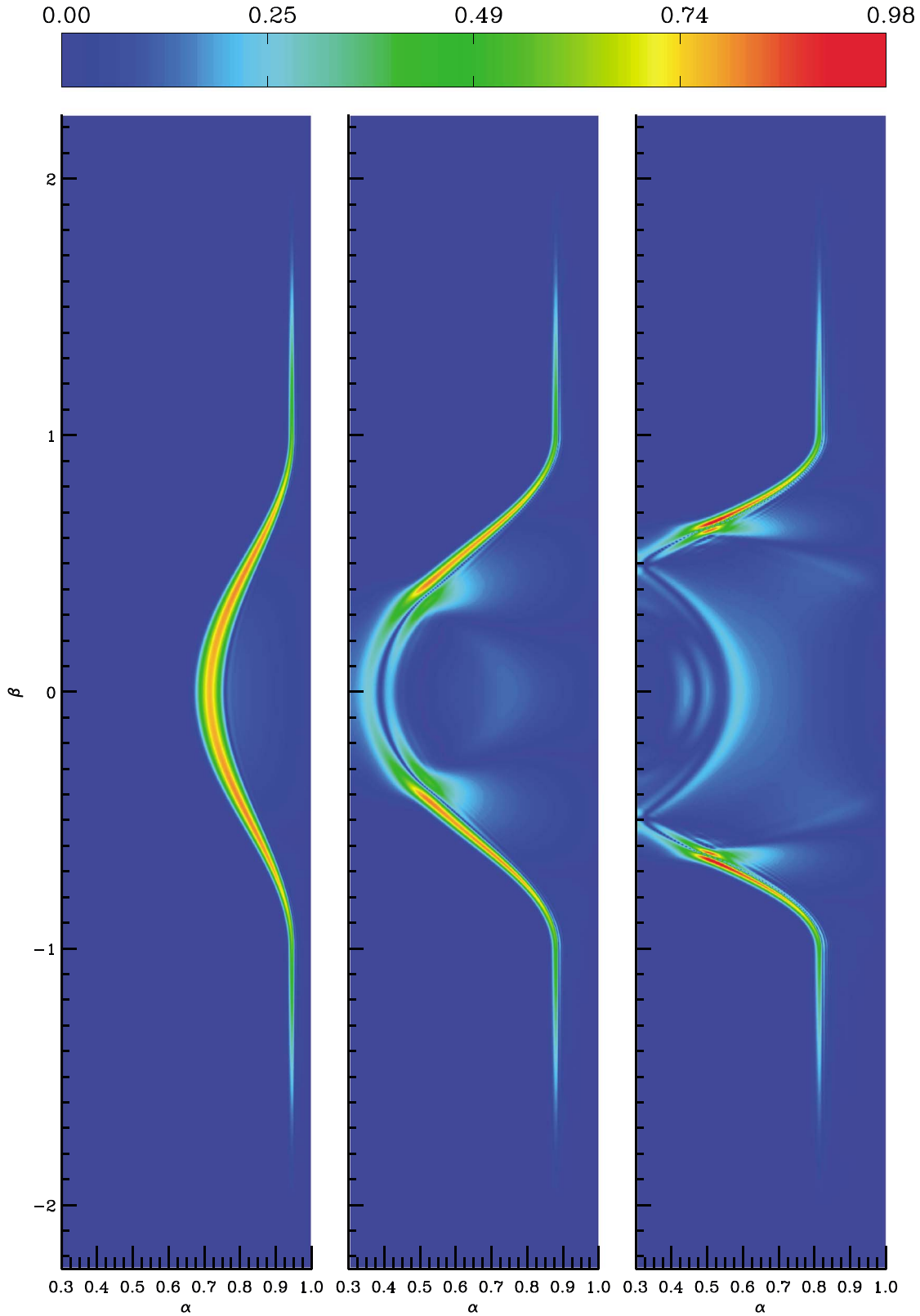

Figure 10. Color-shaded plots of $|b_y|$ in the equatorial plane from the short duration driving simulation at three times: (left) $t = 0.338$, (middle) $t = 0.677$, and (right) $t = 1.015$.

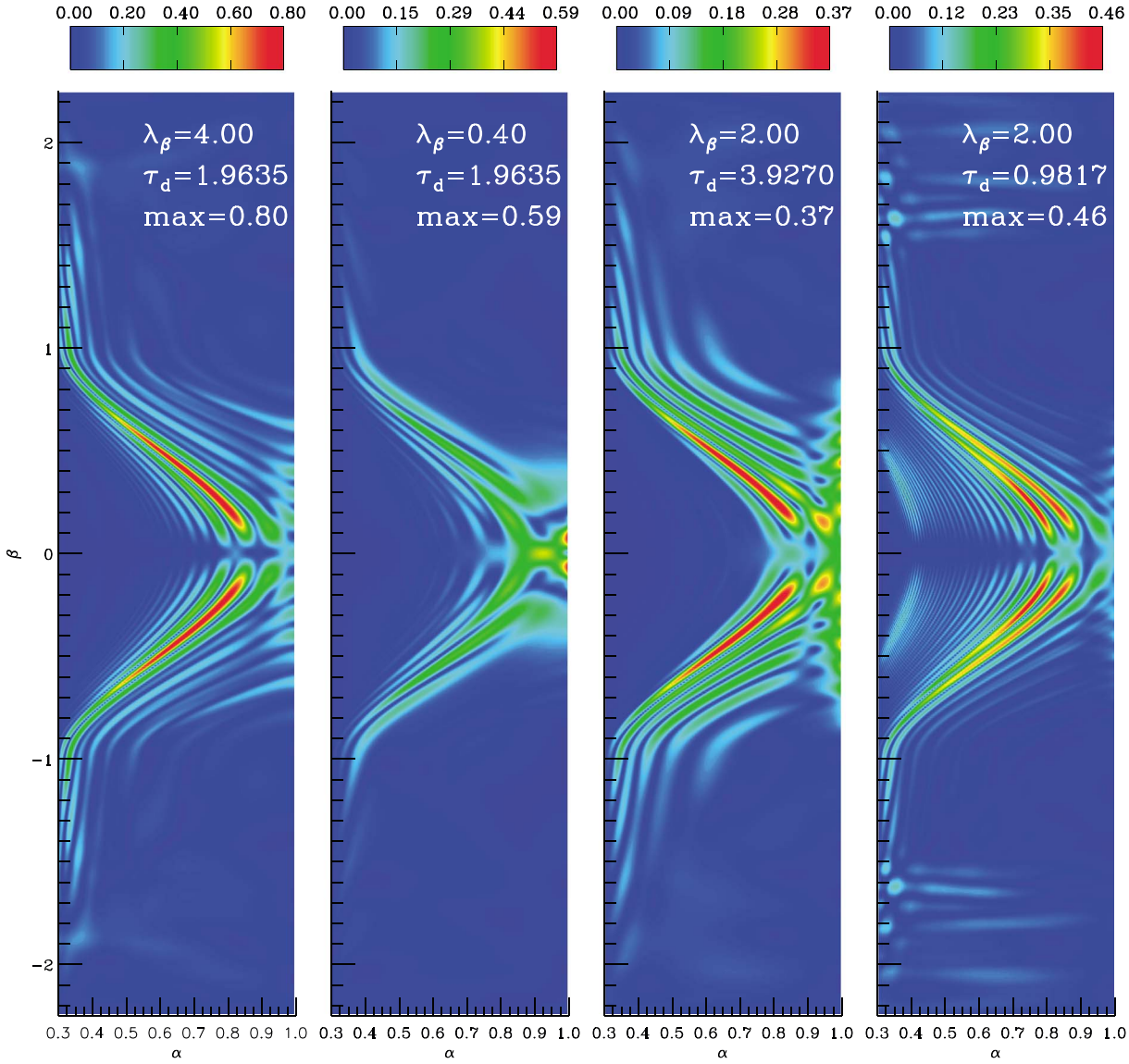

Figure 11. Color-shaded plots of the square root of the kinetic energy ($\sqrt{0.5\rho u^2}$) in the equatorial plane from four simulations with varying driver conditions as annotated in each panel, all at time $t = 12.92$. From left to right: (first panel) larger spatial scale ($\lambda_\beta = 4$); (second panel) shorter spatial scale ($\lambda_\beta = 0.4$); (third panel) longer duration driver ($\tau_d = 3.9270$); (fourth panel) shorter duration ($\tau_d = 0.9817$). For reference, the main simulation sets $\lambda_\beta = 2$, $\tau_d = 1.9635$.

3.5. Varying the Driving Conditions

The final point of consideration is to study how changing the driver parameters affects the mode coupling. To this end we consider changing the spatial and temporal scales of the driver. Figure 11 displays the square root of the kinetic energy in the equatorial plane (as in Figure 4) from four simulations with varying driving conditions. In all cases, the driver is still a "push" to the domain with a perturbation of b_y; however, the duration and spatial scale of this stimulus change in each simulation. We consider a longer (Figure 11, first panel) and shorter (Figure 11, second panel) spatial scale of the driver than the main simulation run from Figure 11 but with the same driving duration. We then change the temporal variation of the driver retaining the spatial variation of the main run, to a longer (Figure 11, third panel) and shorter (Figure 11, fourth panel) duration. The particular parameters for each run can be found in the figure caption and plot annotations.

The striking feature of these simulations is that in all of the cases there is a resonant response at the same location as in the main simulation run. This reveals that the resonance structure and location are inherently properties of the medium, which will be revealed given some broadband stimulus. This medium supports a particular fast waveguide eigenfrequency ($f \sim 0.39$), which therefore drives resonances at the same location

in each simulation, regardless of the changes to the driver. This is a point of major importance, that a driving disturbance can lie within a broad range of temporal and spatial scales and still excite resonances at the same location. This gives credence to the use of the Resonance Map as a diagnostic for the resonance location, as it explains where resonances will form for a given driving frequency. Given that this driving frequency will be the fast waveguide eigenfrequency for all types of broadband driving, the resonance location can then be accurately predicted once this frequency is known.

The other point of interest is how efficient the mode coupling is for each type of driving. Analyzing the amplitudes shown above the color bars in each panel of Figure 11 (also annotated as "max" in each panel) reveals that some of the cases are far more efficient than others. Considering the first two panels comparing different spatial scales of driving, the amplitude discrepancy is unsurprising. In the first, much more energy is put into the domain as the perturbation exists over 10 times the length of that in the second panel. We also note that the maximum value in the second panel is not actually a resonant response, but exists at the driven boundary. The resonant excitation is similar in Figures 11 (third panel) and 11 (fourth panel) since the driving durations are of the same order. The basic requirement is that the spatial scale of the driver is on the order of the length of the domain, and the duration of driving is on the order of the Alfvén crossing time. This will produce the most efficient resonant excitation via the fast waveguide eigenmode.

4. Discussion and Conclusions

The main simulation presented in this paper has addressed two important features of 3-D Alfvén resonance excitation. First, how does a broadband stimulus affect the structure and location of the resonance? Second, can resonances be formed in 3-D in equilibria that are far from axisymmetric and with the FLRs far from being toroidally polarized?

To approach the first problem, we drove the system with a pulse of the field-aligned magnetic field perturbation b_γ. This modeled a push to the domain with a change of magnetic pressure. We observed that with this type of driving the dominant fast frequency is the natural waveguide eigenfrequency, and it is at this frequency that the main resonant response occurs. Given the broadband input, resonances appear over a spatial range dependent upon the frequency bandwidth of the driver. We found resonance excitation to be prevalent at frequencies within the full width at half maximum of the waveguide frequency peak.

We demonstrated how in an inhomogeneous medium, where the poloidal and toroidal Alfvén eigenfrequencies are different, the Resonance Map (WE2016) can be used to determine the location and structure of the resonance, given a dominant driving frequency. In the cases presented, either the boundary conditions or regions where the Alfvén speed is invariant in β can be used to identify where the main resonant response will occur. This follows from the analysis of WE2016.

Through varying the spatial and temporal scales of the driver, we found that the resonances remained at the same locations, albeit with differing amplitudes. Therefore, for a broadband driver which will dominantly excite the fast waveguide mode, the resonance location is given by the Resonance Map constructed using the waveguide frequency. This means that the resonances are a property of the medium, and their observation can be used seismologically to infer properties of the equilibrium, which is an extremely powerful result.

The second problem of highly inclined resonances was addressed by introducing a steep Alfvén speed profile in the azimuthal direction. This forced the resonances in the lower Alfvén speed regions to tunnel radially inward toward higher-frequency regions. Despite the severity of the incline, resonances still formed efficiently, which is perhaps surprising given the previous 2-D theory of purely toroidal resonances in the low azimuthal wave number limit.

We further identified several other key aspects which affect the efficiency of the resonance excitation: gradients in the magnetic pressure which can be produced by wave refraction, persistence of the driver and the evanescence of the fast mode. These properties are vital in understanding what the amplitudes of the resonances will be. We have shown in the main simulation, that steeper gradients at certain locations help to create resonances farther into the evanescent tail of the fast mode of similar amplitude to those farther radially outward.

The work presented here can be extended in several ways to answer important topical questions. For example, what sort of resonances will be produced by realistic variations in the Alfvén speed profile in the Earth's

magnetosphere? Recent work has suggested that there can be large variations in the frequencies observed between the dusk and dawn magnetospheric flanks (Takahashi et al., 2016), which would be directly relevant to the modeling presented here. Furthermore, including a realistic radial Alfvén speed profile will greatly affect the properties of the fast waveguide eigenmodes (Archer et al., 2015, 2017). Finally, what difference does the location of the driver on the magnetopause boundary make to the resonance excitation? In this paper we have only investigated symmetric driving in a symmetric waveguide. Considering realistic terrestrial asymmetries will be the subject of future work.

Acknowledgments
T. Elsden and A. N. Wright were funded by the Leverhulme Trust through Research grant RPG-2016-071. A. N. Wright was also funded by STFC through Consolidated grant ST/N000609/1. Data from simulation results are available on Figshare: https://figshare.com/authors/Tom_Elsden/4743264.

References

Allan, W., Poulter, E. M., & White, S. P. (1986). Hydromagnetic wave coupling in the magnetosphere—Plasmapause effects on impulse-excited resonances. *Planetary Space Science*, *34*, 1189–1200. https://doi.org/10.1016/0032-0633(86)90056-5

Allan, W., White, S. P., & Poulter, E. M. (1985). Magnetospheric coupling of hydromagnetic waves—Initial results. *Geophysical Research Letters*, *12*, 287–290. https://doi.org/10.1029/GL012i005p00287

Allan, W., White, S. P., & Poulter, E. M. (1986). Impulse-excited hydromagnetic cavity and field-line resonances in the magnetosphere. *Planetary Space Science*, *34*, 371–385. https://doi.org/10.1016/0032-0633(86) 90144-3

Archer, M. O., Hartinger, M. D., Walsh, B. M., & Angelopoulos, V. (2017). Magnetospheric and solar wind dependences of coupled fast-mode resonances outside the plasmasphere. *Journal of Geophysical Research: Space Physics*, *122*, 212–226. https://doi.org/10.1002/2016JA023428

Archer, M. O., Hartinger, M. D., Walsh, B. M., Plaschke, F., & Angelopoulos, V. (2015). Frequency variability of standing Alfvén waves excited by fast mode resonances in the outer magnetosphere. *Geophysical Research Letters*, *42*, 10,150–10,159. https://doi.org/10.1002/2015GL066683

Chen, L., & Hasegawa, A. (1974). A theory of long-period magnetic pulsations: 1. Steady state excitation of field line resonance. *Journal of Geophysical Research*, *79*, 1024–1032. https://doi.org/10.1029/JA079i007p01024

Claudepierre, S. G., Hudson, M. K., Lotko, W., Lyon, J. G., & Denton, R. E. (2010). Solar wind driving of magnetospheric ULF waves: Field line resonances driven by dynamic pressure fluctuations. *Journal of Geophysical Research*, *115*, A11202. https://doi.org/10.1029/2010JA015399

Claudepierre, S. G., Toffoletto, F. R., & Wiltberger, M. (2016). Global MHD modeling of resonant ULF waves: Simulations with and without a plasmasphere. *Journal of Geophysical Research: Space Physics*, *121*, 227–244. https://doi.org/10.1002/2015JA022048

Degeling, A. W., Rankin, R., Kabin, K., Rae, I. J., & Fenrich, F. R. (2010). Modeling ULF waves in a compressed dipole magnetic field. *Journal of Geophysical Research*, *115*, A10212. https://doi.org/10.1029/2010JA015410

Dungey, J. W. (1954). Electrodynamics of the outer atmosphere: Report to National Science Foundation on work carried on under grant NSF-G450 (Scientific Report): Ionospheric Research, Ionosphere Research Labor, The Pennsylvania State University, Pennsylvania State University, Ionosphere Research Laboratory.

Dungey, J. W. (1967). Hydromagnetic waves. In S. Matsushita (Ed.), *Physics of Geomagnetic Phenomena* (Vol. 1, pp. 913). New York: Academic Press.

Ellington, S. M., Moldwin, M. B., & Liemohn, M. W. (2016). Local time asymmetries and toroidal field line resonances: Global magnetospheric modeling in SWMF. *Journal of Geophysical Research: Space Physics*, *121*, 2033–2045. https://doi.org/10.1002/2015JA021920

Elsden, T., & Wright, A. N. (2017). The theoretical foundation of 3-D Alfvén resonances: Time-dependent solutions. *Journal of Geophysical Research: Space Physics*, *122*, 3247–3261. https://doi.org/10.1002/2016JA023811

Heyvaerts, J., & Priest, E. R. (1983). Coronal heating by phase-mixed shear Alfven waves. *Astronomy and Astrophysics*, *117*, 220–234.

Inhester, B. (1987). Numerical modeling of hydromagnetic wave coupling in the magnetosphere. *Journal of Geophysical Research*, *92*, 4751–4756. https://doi.org/10.1029/JA092iA05p04751

Ionson, J. A. (1978). Resonant absorption of Alfvenic surface waves and the heating of solar coronal loops. *Astrophysical Journal*, *226*, 650–673. https://doi.org/10.1086/156648

Kaneko, T., Goossens, M., Soler, R., Terradas, J., Van Doorsselaere, T., Yokoyama, T., & Wright, A. N. (2015). Apparent cross-field superslow propagation of magnetohydrodynamic waves in solar plasmas. *Astrophysical Journal*, *812*(2), 121. https://doi.org/10.1088/0004-637X/812/2/121

Keiling, A., Lee, D.-H., & Nakariakov, V. (2016). *Low-frequency waves in space plasmas, Geophysical Monograph Series* (Vol. 216). Washington, DC: American Geophysical Union.

Kivelson, M. G., & Southwood, D. J. (1985). Resonant ULF waves—A new interpretation. *Geophysical Research Letters*, *12*, 49–52. https://doi.org/10.1029/GL012i001p00049

Kivelson, M. G., & Southwood, D. J. (1986). Coupling of global magnetospheric MHD eigenmodes to field line resonances. *Journal of Geophysical Research*, *91*, 4345–4351. https://doi.org/10.1029/JA091iA04p04345

Klimushkin, D. Y., Leonovich, A. S., & Mazur, V. A. (1995). On the propagation of transversally small-scale standing Alfven waves in a three-dimensionally inhomogeneous magnetosphere. *Journal of Geophysical Research*, *100*, 9527–9534. https://doi.org/10.1029/94JA03233

Lee, D.-H., & Lysak, R. L. (1989). Magnetospheric ULF wave coupling in the dipole model—The impulsive excitation. *Journal of Geophysical Research*, *94*, 17,097–17,103. https://doi.org/10.1029/JA094iA12p17097

Lee, D.-H., & Lysak, R. L. (1990). Effects of azimuthal asymmetry on ULF waves in the dipole magnetosphere. *Geophysical Research Letters*, *17*, 53–56. https://doi.org/10.1029/GL017i001p00053

Leonovich, A. S., & Mazur, V. A. (1993). A theory of transverse small-scale standing Alfven waves in an axially symmetric magnetosphere. *Planetary and Space Science*, *41*, 697–717. https://doi.org/10.1016/0032-0633(93)90055-7

Mann, I. R., Wright, A. N., & Cally, P. S. (1995). Coupling of magnetospheric cavity modes to field line resonances: A study of resonance widths. *Journal of Geophysical Research*, *100*, 19,441–19,456. https://doi.org/10.1029/95JA00820

Radoski, H. R. (1967). A note on oscillating field lines. *Journal of Geophysical Research*, *72*, 418–419. https://doi.org/10.1029/JZ072i001p00418

Raes, J. O., Van Doorsselaere, T., Baes, M., & Wright, A. N. (2017). Observations of apparent superslow wave propagation in solar prominences. *Astronomy and Astrophysics*, *602*, A75. https://doi.org/10.1051/0004-6361/201629431

Rickard, G. J., & Wright, A. N. (1994). Alfven resonance excitation and fast wave propagation in magnetospheric waveguides. *Journal of Geophysical Research*, *99*, 13,455–13,464. https://doi.org/10.1029/94JA00674

Samson, J. C., Harrold, B. G., Ruohoniemi, J. M., Greenwald, R. A., & Walker, A. D. M. (1992). Field line resonances associated with MHD waveguides in the magnetosphere. *Geophysical Research Letters*, *19*, 441–444. https://doi.org/10.1029/92GL00116

Samson, J. C., Jacobs, J. A., & Rostoker, G. (1971). Latitude-dependent characteristics of long-period geomagnetic micropulsations. *Journal of Geophysical Research*, *76*, 3675–3683. https://doi.org/10.1029/JA076i016p03675

Singer, H. J., Southwood, D. J., Walker, R. J., & Kivelson, M. G. (1981). Alfven wave resonances in a realistic magnetospheric magnetic field geometry. *Journal of Geophysical Research*, *86*, 4589–4596. https://doi.org/10.1029/JA086iA06p04589

Southwood, D. J. (1974). Some features of field line resonances in the magnetosphere. *Planetary Space Science*, *22*, 483–491. https://doi.org/10.1016/0032-0633(74)90078-6

Takahashi, K., Lee, D.-H., Merkin, V. G., Lyon, J. G., & Hartinger, M. D. (2016). On the origin of the dawn-dusk asymmetry of toroidal Pc5 waves. *Journal of Geophysical Research: Space Physics*, *121*, 9632–9650. https://doi.org/10.1002/2016JA023009

Tamao, T. (1965). Transmission and coupling resonance of hydromagnetic disturbances in the non-uniform Earth's magnetosphere. *Scince Report, Tohoku University, Geophysics*, *17*, 43–72.

Terradas, J., Soler, R., Luna, M., Oliver, R., Ballester, J. L., & Wright, A. N. (2016). Solar prominences embedded in flux ropes: Morphological features and dynamics from 3D MHD simulations. *Astrophysical Journal*, *820*, 1–14. https://doi.org/10.3847/0004-637X/820/2/125

Tirry, W. J., & Goossens, M. (1995). Dissipative MHD solutions for resonant Alfvén waves in two-dimensional poloidal magnetoplasmas. *Journal of Geophysical Research*, *100*, 23,687–23,694. https://doi.org/10.1029/95JA02691

Trottenberg, U., Oosterlee, C., & Schüller, A. (2001). *Multigrid*. London: Academic Press.

Wright, A. N. (1994). Dispersion and wave coupling in inhomogeneous MHD waveguides. *Journal of Geophysical Research*, *99*, 159–167. https://doi.org/10.1029/93JA02206

Wright, A. N., & Allan, W. (1996). Structure, phase motion, and heating within Alfvén resonances. *Journal of Geophysical Research*, *101*, 17,399–17,408. https://doi.org/10.1029/96JA01141

Wright, A. N., & Elsden, T. (2016). The theoretical foundation of 3D Alfvén resonances: Normal modes. *Astrophysical Journal*, *833*, 230. https://doi.org/10.3847/1538-4357/833/2/230

Wright, A. N., & Rickard, G. J. (1995). A numerical study of resonant absorption in a magnetohydrodynamic cavity driven by a broadband spectrum. *Astrophysical Journal*, *444*, 458–470. https://doi.org/10.1086/175620

Wright, A. N., & Thompson, M. J. (1994). Analytical treatment of Alfvén resonances and singularities in nonuniform magnetoplasmas. *Physics of Plasmas*, *1*, 691–705. https://doi.org/10.1063/1.870815

Wright, A. N., Allan, W., Elphinstone, R. D., & Cogger, L. L. (1999). Phase mixing and phase motion of Alfvén waves on tail-like and dipole-like magnetic field lines. *Journal of Geophysical Research*, *104*, 10,159–10,176. https://doi.org/10.1029/1999JA900018

Zalesak, S. T. (1979). Fully multidimensional flux-corrected transport algorithms for fluids. *Journal of Computational Physics*, *31*, 335–362. https://doi.org/10.1016/0021-9991(79)90051-2